

Relative Pose Estimation for Alignment of Long Cylindrical Components Based on Microscopic Vision

Song Liu, De Xu, *Senior Member, IEEE*, Fangfang Liu, Dapeng Zhang, and Zhengtao Zhang, *Member, IEEE*

Abstract—In this paper, an efficient relative pose estimation method based on multimicroscopic vision is presented for the alignment of long cylindrical components in six degree-of-freedom in the 3-D space. First, the relative pose estimation method measures the relative orientation errors between components in a coarse-to-fine manner. The coarse relative orientation estimation reflects the average orientation difference among multiedges and it promises the relative orientation errors can converge to a limited extent rapidly. The fine relative orientation estimation is to detect whether the components will interfere with each other in the insertion process and it provides higher orientation measurement accuracy under multilateral constraint circumstance. The method to determine the invisible feature lines of long cylindrical components of prism shape with odd edges for relative position error estimation is discussed in detail. Afterward, the relative position between components is measured by side-view cameras using the feature lines. In addition, the method to calibrate the optical axis of microscopic camera is also presented. The relative pose estimation method can reliably estimate the relative pose between long cylindrical components of prism shape with odd edges. Alignment experiments and results demonstrate the effectiveness of the proposed relative pose estimation method.

Index Terms—3-D alignment, assembly, feature extraction, image Jacobian matrix, long cylindrical components, multimicroscopic vision, optical axis calibration, relative pose estimation, vision sensing.

I. INTRODUCTION

ASSEMBLY and manipulation in high precision have drawn more and more attention in the domain of advanced manufacturing due to its significant advantages in the fields of photoelectronic engineering, biotechnology, medical science,

and microelectromechanism system [1]–[4]. In the field of precision assembly, the peg-in-hole assembly is a canonical and most frequent assembly operation [5]. Up to now, different relative pose estimation methods together with alignment strategies and assembly systems have been developed to realize the aligning and assembly for different peg-in-hole components. As one of the common and main terms in the domain of precision assembly, the assembly of long cylindrical components of prism shape with odd edges has not been sufficiently investigated. This kind of components is very common in the radar antenna systems, normally known as traveling wave tube (TWT) [6], [7]. As a high-frequency module, the heat dissipation capability of TWT has always been the focus in TWT fabrication, because the heat dissipation capability affects the performance of TWT in loss and efficiency [8], [9]. The main influence factor that determines the heat dissipation capability of TWT is the fabrication accuracy [10]. Traditionally, TWT is fabricated manually, which is difficult to ensure high assembly accuracy. Therefore, it is necessary to develop effective alignment strategy for the assembly of long cylindrical components, and as the basis for alignment progress, relative pose estimation for long cylindrical components always comes first and is worthy of deep investigation.

Precision assembly can be viewed as sequences of precision manipulation with the objective of assembling components together, which can be classified into parallel assembly and serial assembly [11]. Compared with the parallel assembly, serial assembly has much lower efficiency. However, serial assembly is more suited for the production of complex microsystem with more functions, for its ability of assembling microparts of varying shapes and types with high precision and flexibility [12]. For serial assembly, the assembly task can be divided into two subtasks, such as alignment and insertion generally [13]. The alignment is to make sure the components have the same pose in Cartesian space and are ready for insertion.

Traditionally, microscopic vision is necessary for precision assembly system for it offers essential observation methods for precision assembly with a noncontact manner [14]. Many researches have been reported for measurement and control of components' position and pose [15], autofocus algorithm [16], depth information acquisition [17], and vision system calibration and control methods [18] based on microscopic vision. Microscopic vision follows the pin-hole model, whose imaging process can be explained by perspective projection [31]. Since microscopic vision has low depth of field and small field of view (FOV), perspective projection degrades to

Manuscript received November 30, 2014; revised June 17, 2015, August 19, 2015, October 9, 2015, and November 29, 2015; accepted December 3, 2015. Date of publication December 10, 2015; date of current version April 28, 2016. Recommended by Technical Editor F. Aghili. This work was supported in part by the National Natural Science Foundation of China under Grant 61227804, Grant 61421004, Grant 61303177, and Grant 61305115.

The authors are with the Research Center of Precision Sensing and Control, Institute of Automation, Chinese Academy of Sciences, Beijing 100190, China (e-mail: sdliusong@outlook.com; sdxude@yahoo.com; fangfang.liu@ia.ac.cn; dapeng.zhang@ia.ac.cn; zhengtao.zhang@ia.ac.cn).

Color versions of one or more of the figures in this paper are available online at <http://ieeexplore.ieee.org>.

Digital Object Identifier 10.1109/TMECH.2015.2506906

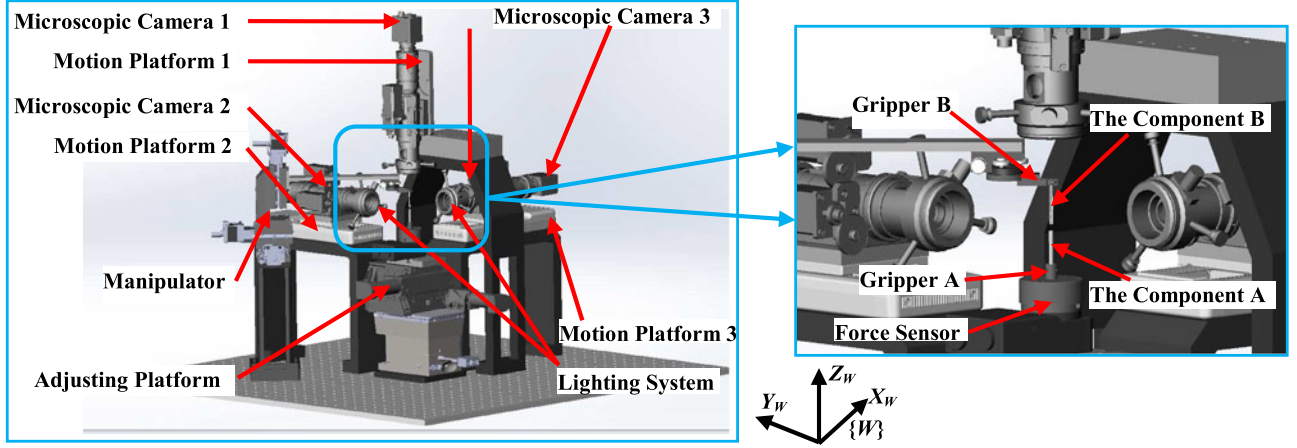


Fig. 1. System Configuration Scheme.

weak-perspective projection in this case. If the zoom factor of the optical lens is one, the weak-perspective projection works in the same way with the orthogonal projection. In addition, it is well known that one microscopic camera can only reliably measure one degree-of-freedom (DOF) rotation and 2-DOF translation [19]. Three microscopic cameras at least are required to measure the component's pose in 6-DOF, and it is sure that the translation measurement for the three microscopic cameras has redundant information. Thus, in order to effectively fuse the information extracted by multimicroscopic vision and sufficiently utilize the redundant information, the vision system needs to be calibrated.

As the basis of alignment, many pose estimation methods have been reported based on microscopic cameras. For example, a relative pose estimation method based on pattern matching is proposed in [20]. In [21], a target recognition method-based oriented fast and rotated brief [22] which has better real-time performance than template matching and pattern clarification is also reported. In [23], a relative pose estimation method based on the CAD model is presented. These methods require the target components both in the FOV of microscopic vision at the same time. For long cylindrical components whose axis scale is at least five as large as its radial scale, this condition cannot be satisfied. Besides, the systems developed on these methods normally have one or two cameras. They are more suitable for planar assembly, but not suitable for pose estimation in 6-DOF in 3-D space, because one camera is only sensitive to one rotation DOF. In [24]–[26], the poses of components are directly measured in the Cartesian space first and then the pose differences are computed. The measurement precision accuracy of this method is highly dependent on the calibration accuracy of the camera intrinsic and extrinsic parameters. Due to the inherent low DOF and small FOV of microscopic cameras, it is not easy to calibrate these parameters. In our previous work [13] and [15], relative pose estimation methods for cylindrical structure components and thin annular structure silicon components are presented. In the methods, the relative position in X - and Y -directions is estimated by a top-view microscopic camera. Using these methods for alignment for long cylindrical

components, the rotation axes of components need to be parallel to the optical axis of the top view camera, and this condition is hard to be guaranteed. The main challenge in relative pose estimation for long cylindrical components of prism shape with odd edges is to determine the invisible feature lines for pose measurement, whose central lines relative to the edge lines projected on the image plane vary with the projection directions. It is necessary to develop relative pose estimation method for the assembly of long cylindrical components.

The motivation of this study is to develop a generalized and easy-to-implement relative pose estimation method for the alignment of long cylindrical components with prism shape of odd edges in the 3-D Cartesian space. The proposed relative pose estimation method needs the microscopic vision system calibrated in advance. Apart from the image Jacobian matrices, the calibration information also involves the direction of the optical axis of the microscopic cameras, which can be directly derived from the translation image Jacobian matrix. The proposed relative pose estimation method first measures the relative orientation errors between components in a coarse-to-fine manner to provide higher orientation measurement accuracy under multilateral constraints circumstance. Then, the invisible feature lines of long cylindrical component for relative position measurement are determined. Afterward, the relative position errors are estimated for the following position alignment. With the proposed relative pose estimation method, automatic alignment can be achieved with hardware system configuration requirements in which three microscopic cameras, a three translation DOF manipulator, and a three rotation DOF adjusting platform are needed.

The rest of this paper is organized as follows. Section II first gives an introduction of the system setup and the components to be aligned. In Section III, the image Jacobian matrices used in this paper and the techniques to calibrate the optical axis of microscopic camera are provided. Then, details of relative pose estimation method are elaborately presented. The alignment scheme and procedure for the alignment experiment are described in Section IV. Section V presents the experiments and results. Finally, this paper is concluded in Section VI.

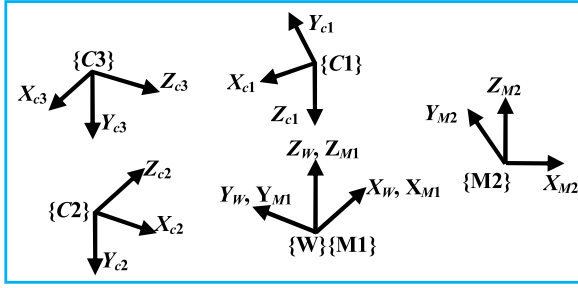


Fig. 2. Coordinates system.

II. SYSTEM AND COMPONENTS

A. System Configuration and Calibration

The automated precision alignment system is designed as given in Fig. 1. It consists of a three translation DOF manipulator, a three rotation DOF adjusting platform, three optical microscopic cameras, corresponding lighting system, and a host computer. The three optical axes of the microscopic cameras are approximately orthogonal to each other. All three microscopic cameras can be moved along their moving platforms on support mechanisms to adjust the distance between the objective lens and components in order to capture clear images. The host computer is used to control the whole alignment procedure including capturing images from the microscopic cameras, image processing and controlling the adjusting platform, and manipulator to align the two components.

The coordinates are established, as shown in Fig. 2. The world coordinates $\{W\}$ and the manipulating coordinates $\{M1\}$ are established on the adjusting platform. Manipulation coordinates $\{M2\}$ is established on the manipulator. The camera coordinates $\{C1\}$, $\{C2\}$, and $\{C3\}$ are established with origins being their optical centers. The X - and Y -axes of $\{C1\}$, $\{C2\}$, and $\{C3\}$ are along u - and v -axes of their images. The Z -axes of $\{C1\}$, $\{C2\}$, and $\{C3\}$ point from the origins to the scene.

Image Jacobian matrix is the transformation matrix from incremental motion of the features in the Cartesian space to them on images. The image Jacobian matrixes concerned are rotation matrix J_1 and translation matrix J_2 and J_3 as given in (1)–(3), respectively. J_1 represents the transformation from incremental rotation of the feature lines in the Cartesian space to them on images of the three cameras since the adjusting platform rotates the component A . J_2 and J_3 represent the transformation from incremental translation of the feature points in the Cartesian space to them on images since the manipulator moves the component B .

$$\begin{bmatrix} \Delta\theta_{c1} \\ \Delta\theta_{c2} \\ \Delta\theta_{c3} \end{bmatrix} = \begin{bmatrix} J_{111} & J_{112} & J_{113} \\ J_{121} & J_{122} & J_{123} \\ J_{131} & J_{132} & J_{133} \end{bmatrix} \begin{bmatrix} \Delta\theta_x \\ \Delta\theta_y \\ \Delta\theta_z \end{bmatrix} = J_1 \begin{bmatrix} \Delta\theta_x \\ \Delta\theta_y \\ \Delta\theta_z \end{bmatrix} \quad (1)$$

where $\Delta\theta_{c1}$, $\Delta\theta_{c2}$, and $\Delta\theta_{c3}$ are the incremental angles on images captured by the microscopic cameras 1, 2, and 3, respectively; $\Delta\theta_x$, $\Delta\theta_y$, and $\Delta\theta_z$ are the incremental rotation angles

of the component A around X_w , Y_w , and Z_w axis, respectively

$$\begin{bmatrix} \Delta u_{c1} \\ \Delta v_{c1} \end{bmatrix} = \begin{bmatrix} J_{211} & J_{212} & J_{213} \\ J_{221} & J_{222} & J_{223} \end{bmatrix} \begin{bmatrix} \Delta x_{m2} \\ \Delta y_{m2} \\ \Delta z_{m2} \end{bmatrix} = J_2 \begin{bmatrix} \Delta x_{m2} \\ \Delta y_{m2} \\ \Delta z_{m2} \end{bmatrix} \quad (2)$$

$$\begin{bmatrix} \Delta u_{c2} \\ \Delta v_{c2} \\ \Delta u_{c3} \\ \Delta v_{c3} \end{bmatrix} = \begin{bmatrix} J_{311} & J_{312} & J_{313} \\ J_{321} & J_{322} & J_{323} \\ J_{331} & J_{332} & J_{333} \\ J_{341} & J_{342} & J_{343} \end{bmatrix} \begin{bmatrix} \Delta x_{m2} \\ \Delta y_{m2} \\ \Delta z_{m2} \end{bmatrix} = J_3 \begin{bmatrix} \Delta x_{m2} \\ \Delta y_{m2} \\ \Delta z_{m2} \end{bmatrix} \quad (3)$$

where $(\Delta u_{c1}, \Delta v_{c1})$, $(\Delta u_{c2}, \Delta v_{c2})$, and $(\Delta u_{c3}, \Delta v_{c3})$ are the coordinates increments of the three feature points on the images of the microscopic cameras 1, 2, and 3, respectively; $(\Delta x_{m2}, \Delta y_{m2}, \Delta z_{m2})$ is the incremental translation of the component B moved by the manipulator. Detailed method to calibrate image Jacobian matrix is available in [13].

The calibration of the optical axis of microscopic camera is to obtain the direction vector of the optical axis with respect to the manipulator coordinates $\{M2\}$. According to the definition of image Jacobian matrix, when a physical feature point is translated along the optical axis of microscopic camera 2 by the manipulator, the image coordinates of the feature point keep constant, which can be expressed by

$$\lambda \begin{bmatrix} J_{311} & J_{312} & J_{313} \\ J_{321} & J_{322} & J_{323} \end{bmatrix} \begin{bmatrix} v_{2x} \\ v_{2y} \\ v_{2z} \end{bmatrix} = \lambda J_{32} V_2 = \begin{bmatrix} 0 \\ 0 \end{bmatrix} \quad (4)$$

where λ is scale factor, J_{32} is formed from the upper two rows of J_3 , and $V_2 = [A_2, B_2, C_2]^T$ is the direction vector of the optical axis of microscopic camera 2 in coordinates $\{M2\}$.

Expression (4) can be rewritten as homogeneous linear equations and J_{32} is the coefficient matrix of the linear equations. Normally, the rank of the matrix J_{32} is 2. Therefore, there is general solution for the linear equations. The method to compute the direction vector of microscopic camera 2 in coordinates $\{M2\}$ goes the same with microscopic camera 3 with J_{32} replaced by J_{33} . J_{33} is formed from the lower two rows of J_3 .

Considering the direction vector V_i of the microscopic camera i as an incremental translation moved by the manipulator, the view direction of the microscopic camera i with respect to microscopic camera 1, denoted as V'_i , can be computed by

$$\begin{bmatrix} \Delta u_{V'_i} \\ \Delta v_{V'_i} \end{bmatrix} = J_2 \begin{bmatrix} A_i \\ B_i \\ C_i \end{bmatrix} \quad (5)$$

where $[\Delta u_{V'_i}, \Delta v_{V'_i}]^T$ is the direction vector V'_i , $i = 2$ and 3 , and i is the microscopic camera's serial number.

B. Components and Task Specification

The components to be aligned are given in Fig. 3. In the center of the component B is a helix with three limit levers attached to the helix by 120° . The height of the component B is 30.0 mm. On the top view, the six corner points of the limit levers are at a circle with diameter of

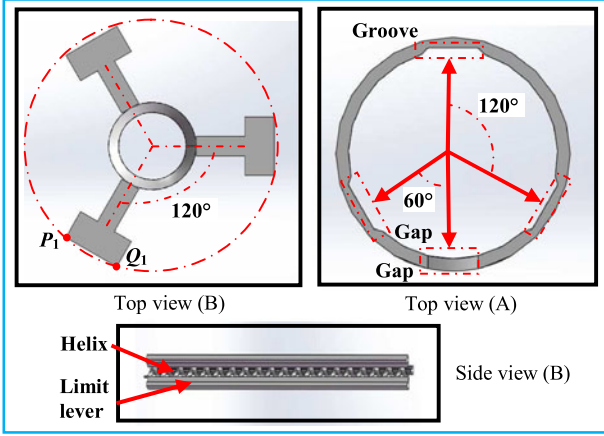


Fig. 3. Component A and component B.

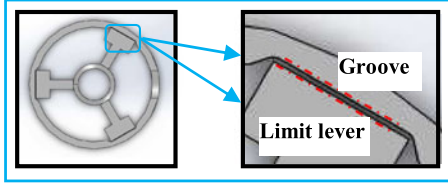


Fig. 4. Top view of the assembled component.

3.0 mm and the diameter of the helix is 1.0 mm. The length of the chord defined by the corner point P_1 and Q_1 is 0.6 mm. The component A is cylindrical structure with three grooves in the inner wall by 120° . The height of the component A is also 30.0 mm. There is a gap at the topside of the component A located in the middle of two grooves. Fig. 4 shows the assembled component. The three limit levers are inserted in the three grooves and the interval between the limit lever and the groove is $10\ \mu\text{m}$.

Our task is to realize the alignment of the component A and the component B in the Cartesian space in 6-DOFs. The alignment procedure is composed of coarse-to-fine-orientation alignment and the following position alignment. Detailed description of the alignment procedure is given in Section IV-B.

III. FEATURE EXTRACTION

A. Feature Extraction for Coarse Relative Orientation Estimation

In the method, image features mainly are lines selected from the two components. For orientation measurement, edge lines are extracted on images captured from microscopic cameras 1, 2, and 3. For position alignment, line features are extracted and estimated on images captured from microscopic cameras 2 and 3.

Fig. 5 shows the line features of the components A and B on the images captured by microscopic camera 1. They are separately extracted from the two images since the image of component A can be only captured by the microscopic camera 1 when the component B is moved away. As shown in Fig. 5, the lines L_{br} and L_{ar} are extracted using progressive probabilistic

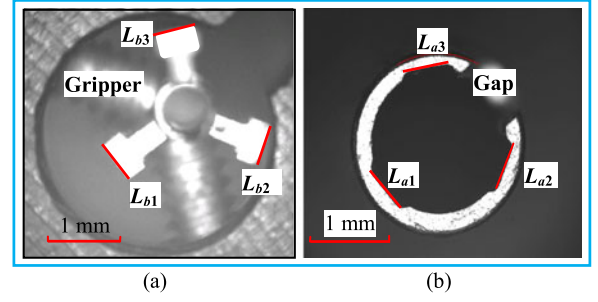


Fig. 5. Line features on images captured by microscopic camera 1 for coarse-orientation alignment. (a) Component B. (b) Component A.

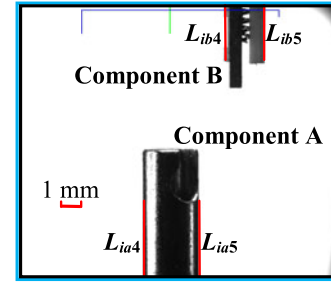


Fig. 6. Feature lines on image captured by microscopic camera 2 for orientation alignment.

Hough transform (PPHT) [27] from the edge points detected by the Canny operator [28] on the images of the two components, $r = 1, 2$, and 3. L_{br} is the external edge line of the limit levers of the component B and L_{ar} is the internal edge line of the grooves of the component A. In this paper, all line equations on image space are expressed by

$$Au + Bv + C = 0. \quad (6)$$

The parameters of line L_{br} and L_{ar} are $A_{br}, B_{br}, C_{br}, A_{ar}, B_{ar},$ and C_{ar} , r is the line index number, $r = 1, 2, 3$. The orientation error $\Delta\theta_{c1}$ for coarse orientation measurement is computed by

$$\Delta\theta_{c1} = \frac{1}{3} \sum_{r=1}^3 [\text{atan2}(-A_{br}, B_{br}) - \text{atan2}(-A_{ar}, B_{ar})]. \quad (7)$$

The line $L_{ib4}, L_{ib5}, L_{ia4},$ and L_{ia5} as shown in Fig. 6 are extracted on the images of the two components captured by the microscopic cameras $i, i = 2, 3$. L_{ib4} and L_{ib5} are side edge lines of the component B, while L_{ia4} and L_{ia5} are the side edge line of the component A. The parameters of line L_{ibr} and L_{iar} on the images of the microscopic camera i are $A_{ibr}, B_{ibr}, C_{ibr}, A_{iar}, B_{iar},$ and C_{ibr} , r is the line index number, $r = 4, 5$, and i is the camera serial number, $i = 2, 3$.

The orientation errors $\Delta\theta_{c2}$ and $\Delta\theta_{c3}$ are computed by

$$\Delta\theta_{ci} = \frac{1}{2} \sum_{r=4}^5 [\text{atan2}(-A_{ibr}, B_{ibr}) - \text{atan2}(-A_{iar}, B_{iar})] \quad (8)$$

where $i = 2, 3$.

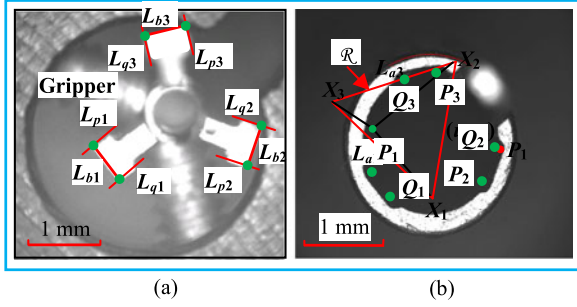


Fig. 7. Line features on image captured by microscopic camera 1 for fine orientation alignment. (a) Component B. (b) Component A.

The orientation errors $\Delta\theta_{c1}$, $\Delta\theta_{c2}$, and $\Delta\theta_{c3}$ are used for coarse-orientation estimation. It should be noted that the orientation error $\Delta\theta_{c1}$ describes the average angle differences between line \mathbf{L}_{br} and \mathbf{L}_{ar} , $r = 1, 2$, and 3 . However, because the interval between outer edge line of the limit lever and the inner edge line of the groove is only $10 \mu\text{m}$, keeping $\Delta\theta_{c1}$ to be minimum cannot promise all three limit levers are exactly involved in the three grooves due to image processing error, alignment control error, or components manufacturing error. Therefore, fine-orientation estimation is conducted to achieve higher measurement precision in orientation around \mathbf{Z}_w axis.

B. Feature Extraction for Fine Relative Orientation Estimation

Features concerned for fine-orientation estimation around \mathbf{Z}_w axis are extracted from images captured from microscopic camera 1, as shown in Fig. 7.

\mathbf{L}_{br} is the external edge line of the limit levers of the component B, $r = 1, 2$, and 3 , as demonstrated in Fig. 5(a). \mathbf{L}_{pr} and \mathbf{L}_{qr} are additional lines extracted from the component B for fine-orientation alignment, $r = 1, 2$, and 3 and their parameters are A_{pr} , B_{pr} , C_{pr} , A_{qr} , B_{qr} , and C_{qr} .

\mathbf{L}_{pr} and \mathbf{L}_{br} intersect with each other on point \mathbf{P}_r . The coordinates on image are computed by (9), $r = 1, 2$, and 3

$$\begin{cases} u_{pr} = \frac{A_{pr}B_{br}C_{br} - A_{br}B_{pr}C_{pr}}{A_{br}A_{pr}B_{br} - A_{br}^2B_{pr}} - C_{br} \\ v_{pr} = \frac{A_{br}C_{pr} - A_{pr}C_{br}}{A_{pr}B_{br} - A_{br}B_{pr}} \end{cases} \quad (9)$$

where (u_{pr}, v_{pr}) are the coordinates of \mathbf{P}_r , $r = 1, 2$, and 3 . \mathbf{L}_{qr} and \mathbf{L}_{br} intersect with each other on point \mathbf{Q}_r . Similarly, the coordinates, (u_{qr}, v_{qr}) , of \mathbf{Q}_r can be computed.

The projection region of the component A on images captured by microscopic camera 1, here denoted as \mathcal{R} , is segmented using an Ostu method [29]. The \mathcal{R} is a set of pixels. The target of fine-orientation alignment is to make sure that no \mathbf{P}_r or \mathbf{Q}_r is

involved in \mathcal{R} , $r = 1, 2$, and 3 . Since \mathbf{P}_r , \mathbf{Q}_r , and \mathcal{R} are extracted from different images captured from microscopic camera 1, \mathbf{P}_r and \mathbf{Q}_r first need to be translated to make the sum of the distance from point \mathbf{P}_r and \mathbf{Q}_r to line \mathbf{L}_{ar} , as expressed by (10), be minimum

$$S(u_t, v_t) = \sum_{r=1}^3 \frac{|A_{ar}(u_{pr} - u_t) + B_{ar}(v_{pr} - v_t) + C_{ar}|}{\sqrt{A_{ar}^2 + B_{ar}^2}} + \sum_{r=1}^3 \frac{|A_{ar}(u_{qr} - u_t) + B_{ar}(v_{qr} - v_t) + C_{ar}|}{\sqrt{A_{ar}^2 + B_{ar}^2}} \quad (10)$$

where u_t and v_t are the translation factor along \mathbf{u}_1 - and \mathbf{v}_1 -axis on image, $r = 1, 2$, and 3 . The resolution of (10) is given as

$$\min_{u_t, v_t} S = S(u_t, v_t) \Big|_{\frac{\partial S^2}{\partial u_t} = 0, \frac{\partial S^2}{\partial v_t} = 0}. \quad (11)$$

After translation, \mathbf{P}_r and \mathbf{Q}_r should not be involved in \mathcal{R} at the same time since there is a $10 \mu\text{m}$ interval between the limit lever and the groove. The orientation error $\Delta\theta_{c1}$ for fine-orientation alignment is computed by Equation (12) as shown at the bottom of the page, where ε is a fixed value, which is set based on the image processing repeatability of orientation feature extraction.

C. Feature Extraction for Relative Position Estimation

Line features used for position alignment is computed after orientation alignment is finished on images captured from microscopic camera i , i is the microscopic camera's serial number, and $i = 2, 3$. Since the component B is nonaxis-symmetrical structure from side view as shown in Fig. 8, while the component A is cylindrical structure, the side edge lines of component A on images captured by microscopic cameras 2 and 3 cannot be directly used to align with the side edge lines of component B.

The side edge lines \mathbf{L}_{ib4} and \mathbf{L}_{ib45} of the component B are used for position alignment. To confirm the corresponding line features of the component A used for position alignment, we first calculate the coordinates of intersection, \mathbf{P}'_r and \mathbf{Q}'_r , of line \mathbf{L}_{pr} and \mathbf{L}_{ar} , line \mathbf{L}_{qr} and \mathbf{L}_{ar} , denoted as (u'_{pr}, v'_{pr}) and (u'_{qr}, v'_{qr}) , using the method in (9), $r = 1, 2$, and 3 .

In Fig. 8, \mathbf{V}'_i is the view direction of the microscopic camera i with respect to the image coordinates of microscopic camera 1, $i = 2, 3$. Viewing the component B from \mathbf{V}'_i , the left-most point of \mathbf{P}'_r and \mathbf{Q}'_r is the projection of line \mathbf{L}_{ib4} ; the right-most point of \mathbf{P}'_r and \mathbf{Q}'_r is the projection of line \mathbf{L}_{ib5} . Similarly, viewing the component A from \mathbf{V}'_i , the left-most point of \mathbf{P}'_r and \mathbf{Q}'_r is the projection of line \mathbf{L}_{is1} ; the right-most point of \mathbf{P}'_r and \mathbf{Q}'_r is the projection of line \mathbf{L}_{is2} , as shown in Fig. 8, i is the microscopic camera's serial number, $i = 2, 3$. After

$$\Delta\theta_{C1} = \begin{cases} \varepsilon & \mathcal{R} \cap \{P_1, P_2, P_3\} \neq \emptyset \quad \text{and} \quad \mathcal{R} \cap \{Q_1, Q_2, Q_3\} = \emptyset \\ 0 & \mathcal{R} \cap \{P_1, P_2, P_3\} = \emptyset \quad \text{and} \quad \mathcal{R} \cap \{Q_1, Q_2, Q_3\} = \emptyset \\ -\varepsilon & \mathcal{R} \cap \{P_1, P_2, P_3\} = \emptyset \quad \text{and} \quad \mathcal{R} \cap \{Q_1, Q_2, Q_3\} \neq \emptyset \end{cases} \quad (12)$$

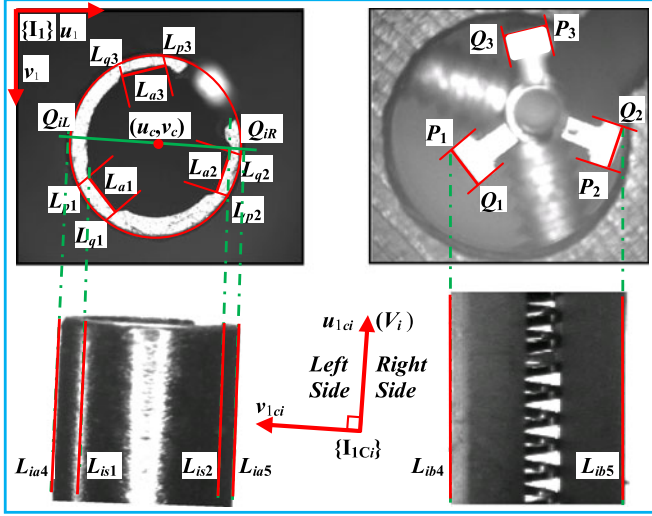


Fig. 8. Line features for position alignment.

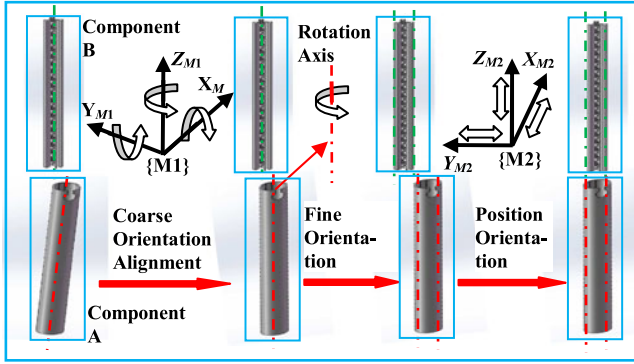


Fig. 9. Alignment Scheme.

fine-orientation alignment, the right-most/left-most point of P'_r and Q'_r is the nearest point on the component A to the right-most/left-most point of P_r and Q_r viewing from microscopic camera 1. Therefore, L_{is1} and L_{is2} are the feature lines of the component A used for position alignment. However, compared with line L_{ib4} and L_{ib5} , L_{is1} and L_{is2} cannot be extracted directly on image. Indeed, L_{is1} and L_{is2} are estimated based on V'_i .

The coordinates of P_r and Q_r , P'_r and Q'_r viewing from V'_i are first converted from coordinates $\{I_1\}$ to coordinates $\{I_{1ci}\}$ by (13) in order to determine the right-most/left-most point. $\{I_1\}$ is image coordinates of camera 1 and $\{I_{1ci}\}$ is the transformed image coordinates formed with V'_i

$$\begin{bmatrix} \bar{u} \\ \bar{v} \end{bmatrix} = \begin{bmatrix} \Delta u_{V'_i} & \Delta v_{V'_i} \\ -\Delta v_{V'_i} & \Delta u_{V'_i} \end{bmatrix} \begin{bmatrix} u \\ v \end{bmatrix} \quad (13)$$

where (u, v) is the image coordinate in $\{I_1\}$, (\bar{u}, \bar{v}) is the image coordinate in $\{I_{1ci}\}$, and $[\Delta u_{V'_i} \ \Delta v_{V'_i}]^T$ is the direction vector V'_i .

Then, converted coordinates of P_r and Q_r , P'_r and Q'_r in the coordinates $\{I_{1ci}\}$ are $(\bar{u}_{pr}, \bar{v}_{pr})$, $(\bar{u}_{qr}, \bar{v}_{qr})$, $(\bar{u}'_{pr}, \bar{v}'_{pr})$ and $(\bar{u}'_{qr}, \bar{v}'_{qr})$, $r = 1, 2, 3$. Then, the converted P_r or Q_r with the largest/smallest \bar{v} coordinate is the left-/right-most point,

while the converted point P'_r or Q'_r with the largest/smallest \bar{v}' coordinate is the left-/right-most point.

The projection of L_{ia4} and L_{ia5} on image captured by microscopic camera 1 is the intersection of the outer counter of the component A and the line parallel to v_{ci} and going through the center of the outer counter, here denoted as Q_{iL} and Q_{iR} .

The parameters of line L_{is1} and L_{is2} are A_{isr} , B_{isr} , and C_{isr} , i is the microscopic camera's serial number, $i = 2, 3$, r is the line index number, $r = 1, 2$. Based on the image Jacobian matrix, the displacement vector of L_{2s1} relative to L_{2a4} , L_{3s1} relative to L_{3a4} can be computed by

$$\begin{bmatrix} \Delta u_{2s1} \\ \Delta v_{2s1} \\ \Delta u_{3s1} \\ \Delta v_{3s1} \end{bmatrix} = J_3 J_2^+ \begin{bmatrix} \bar{u}'_{2pq} - \bar{u}_{2QL} \\ \bar{v}'_{2pq} - \bar{v}_{2QL} \\ \bar{u}'_{3pq} - \bar{u}_{3QL} \\ \bar{v}'_{3pq} - \bar{v}_{3QL} \end{bmatrix} \quad (14)$$

where $[\Delta u_{2s1}, \Delta v_{2s1}]^T$ is the displacement vector of L_{2s1} relative to L_{2a4} , $[\Delta u_{3s1}, \Delta v_{3s1}]^T$ is the displacement vector of L_{3s1} relative to L_{3a4} , $(\bar{u}'_{2pq}, \bar{v}'_{2pq})$ and $(\bar{u}'_{3pq}, \bar{v}'_{3pq})$ are the coordinates of left-most point of P'_r and Q'_r in coordinates $\{I_{1c2}\}$ and $\{I_{1c3}\}$ formed from V'_2 and V'_3 , respectively, and $(\bar{u}_{2QL}, \bar{v}_{2QL})$ and $(\bar{u}_{3QL}, \bar{v}_{3QL})$ are the coordinates of Q_{2L} and Q_{3L} in coordinates $\{I_{1c2}\}$ and $\{I_{1c3}\}$, respectively. Similarly, the displacement vector $[\Delta u_{2s2}, \Delta v_{2s2}]^T$ of L_{2s2} relative to L_{2a5} , and the displacement vector $[\Delta u_{3s2}, \Delta v_{3s2}]^T$ of L_{3s2} relative to L_{3a5} , can be computed.

Once the displacement vectors are calculated, the line parameter C_{is1} and C_{is2} of the line L_{is1} and L_{is2} are determined with $A_{is1} = A_{ia4}$, $B_{is1} = B_{ia4}$, $A_{is2} = A_{ia5}$, and $B_{is2} = B_{ia5}$. Afterward, the position features Δu_{c2} , Δv_{c2} , Δu_{c3} , and Δv_{c3} are computed by

$$\begin{cases} \Delta u_{ci} = \frac{1}{2} \left(\frac{C_{ia4}}{A_{ia4}} + \frac{[\Delta u_{is1} \ \Delta v_{is1}]}{A_{ia4}} \begin{bmatrix} A_{ia4} \\ B_{ia4} \end{bmatrix} + \frac{C_{ia5}}{A_{ia5}} \right. \\ \quad \left. + \frac{[\Delta u_{is2} \ \Delta v_{is2}]}{A_{ia5}} \begin{bmatrix} A_{ia5} \\ B_{ia5} \end{bmatrix} - \frac{C_{ib4}}{A_{ib4}} - \frac{C_{ib5}}{A_{ib5}} \right) \\ \Delta v_{ci} = 0 \end{cases} \quad (15)$$

where $i = 2, 3$.

In (15), Δv_{ci} is set to be zero manually because line L_{is1} , L_{is2} , L_{ib4} , and L_{ib5} are approximately orthogonal to the u -axis of the image coordinates.

IV. AUTOMATIC ALIGNMENT

A. Alignment Scheme

With the relative pose estimation method proposed above, the alignment of long cylindrical components in 3-D space with 6-DOFs is achieved with a two-stage alignment scheme: the coarse-to-fine-orientation alignment and the position alignment, as shown in Fig. 9. The coarse-to-fine-orientation alignment aligns one component to the other in three rotation DOFs, while the position alignment aligns the components in three translation DOFs. Based on the components proposed in this paper, detailed alignment scheme is given as following.

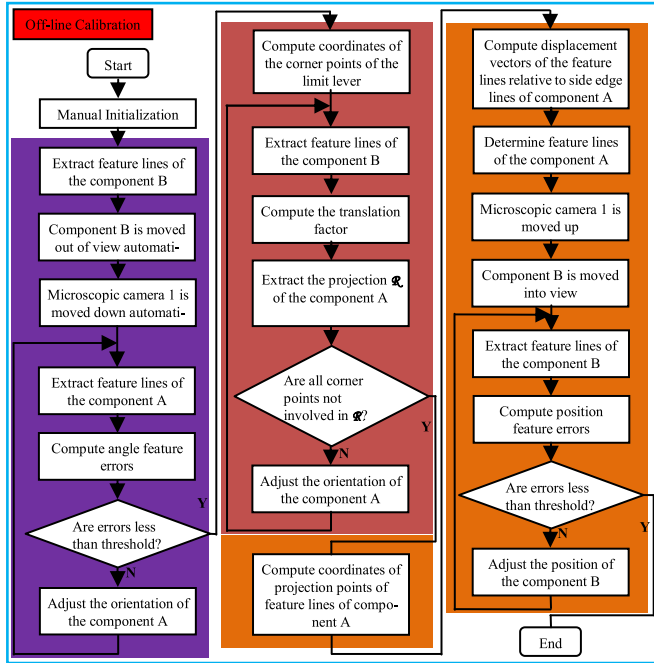


Fig. 10. Alignment Procedure.

The coarse-orientation alignment is to align the component A to the component B by rotating the adjusting platform in coordinates $\{M1\}$, which mainly achieves precision orientation alignment in X_{M1} - and Y_{M1} -axis, and coarse-orientation alignment in Z_{M1} -axis. The target of fine-orientation alignment is mainly to achieve precision orientation alignment in Z_{M1} -axis. The expression (12) cannot tell the angle difference directly since it only offers the error direction information. By rotating the component A around the rotation axis of the component A with a fixed rotation step length, the position of the translated point P_r and Q_r can be modified precisely in the condition they do not involve in the \mathcal{R} , while the orientation errors $\Delta\theta_{c2}$ and $\Delta\theta_{c3}$ are kept unchanged.

After the coarse-to-fine-orientation alignment, the feature line L_{is1} and L_{is2} of the component A used for position alignment is determined and estimated using the view direction vector V'_i discussed in Section III-B. The position alignment is to align the component B to the component A by moving the manipulator along the X_{M2} - and Y_{M2} -axis in coordinates $\{M2\}$.

B. Alignment Procedure

The alignment of the two components A and B is separated to coarse-to-fine-orientation alignment and position alignment, both of which are achieved via visual servo control based on the image Jacobian matrix. The whole alignment process is given in Fig. 10.

First of all in the procedure, the initial poses of the two components are manually adjusted to adequate status. In other words, the component B can be captured clear images by the three microscopic cameras and the component A can be captured clear images by the microscopic cameras 2 and 3. The line L_{br} , L_{pr} , and L_{qr} are extracted from the images

of the component B captured by the microscopic cameras 1. Their parameters A_{br} , B_{br} , A_{pr} , B_{pr} , A_{qr} , and B_{qr} are obtained, $r = 1, 2$, and 3. The line L_{2b4} , L_{2b5} , L_{3b4} , and L_{3b5} are extracted from the images of the component B captured by microscopic cameras 2 and 3, and their parameters of A_{2b4} , B_{2b4} , A_{2b5} , B_{2b5} , A_{3b4} , B_{3b4} , A_{4b5} , and B_{4b5} are obtained. Then, the component B is moved away automatically, which is out of the views of the three microscopic cameras. The microscopic camera 1 is moved down an adequate distance to make images of the component A clear. The line L_{ar} is extracted from images of the component A captured by the microscopic camera 1, $r = 1, 2$, and 3. The parameters A_{ar} and B_{ar} are obtained. The line L_{2a4} , L_{2a5} , L_{3a4} , and L_{3a5} are extracted from the images of the component A captured by microscopic cameras 2 and 3, and their parameters of A_{2a4} , B_{2a4} , A_{2a5} , B_{2a5} , A_{2a4} , B_{2a4} , A_{2a5} , and B_{2a5} are obtained. Then, $\Delta\theta_{c2}$ and $\Delta\theta_{c3}$ are computed with (8) and $\Delta\theta_{c1}$ for coarse-orientation alignment is computed with (7). The orientations of the component A are adjusted by the adjusting platform to realize the coarse-orientation alignment according to the errors $\Delta\theta_{c1}$, $\Delta\theta_{c2}$, and $\Delta\theta_{c3}$.

After coarse-orientation alignment, the coordinates of the corner points of the limit levers of the component B is computed by (9) and the pixel set \mathcal{R} of the component A is segmented on image. In addition, the line L_{ar} is extracted from images of the component A captured by the microscopic camera 1, $r = 1, 2$, and 3 again. Afterward, compute the translation factor introduced in (10) by (11). Then, compute $\Delta\theta_{c1}$ for fine-orientation alignment, and the orientation of the component A is adjusted with the adjusting platform to realize the fine-orientation alignment.

After the coarse-to-fine-orientation alignment is finished, the coordinates of the projection points of feature lines of the component A on images captured by microscopic camera 1 are computed. The displacement vectors of feature line L_{is1} relative to edge line L_{ia4} , feature line L_{is2} relative to edge line L_{ia5} are calculated by (14), i are the microscopic camera's serial number, $i = 2, 3$. Afterward, the feature line L_{is1} and L_{is2} are determined and their parameters A_{isr} , B_{isr} , and C_{isr} are obtained, $r = 1, 2$. The microscopic camera 1 is moved up an adequate distance and the component B is moved into the view of the microscopic cameras 2 and 3. The line L_{2b4} , L_{2b5} , L_{3b4} , and L_{3b5} are extracted from the images of the component B captured by microscopic cameras 2 and 3, and their parameters of A_{2b4} , B_{2b4} , A_{3b5} , and B_{3b5} are obtained. Then, Δu_{c2} , Δv_{c2} , Δu_{c3} , and Δv_{c3} are computed by (15). The position of the component B is adjusted by the manipulator to realize the position alignment according to the errors Δu_{c2} , Δv_{c2} , Δu_{c3} , and Δv_{c3} . The position alignment is finished once the position errors on image are less than the given threshold.

The controllers used for coarse-orientation alignment and position alignment are both PI controllers. Both the manipulator and the operation platform are driven by stepper motors. Since the control object of the system can be described as a first-order inertia element and a first-order integral element, the system can be viewed as a second-order system. Therefore, with the PI parameters being selected properly, the stability of the system

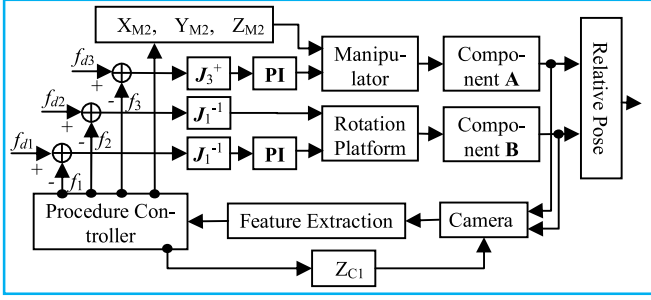


Fig. 11. Diagram of the alignment control system, f_{d1} , f_{d2} and f_{d3} are the expected and current relative orientation features, f_1 , f_2 and f_3 are the expected and current relative position features of the two components.

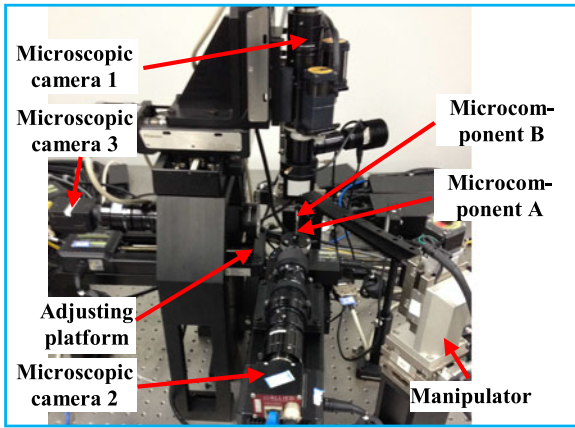


Fig. 12. Experiment system.

can be guaranteed. K_{p1} and K_{i1} are the proportional coefficient and integral coefficient of the coarse-orientation alignment controller, while K_{p3} and K_{i3} are the controller parameters for position alignment. Detailed controller design method can be found in our previous works in [13] and [30]. The block diagram for the control system is given by Fig. 11, in which a procedure controller is deployed to determine which substage, such as the coarse-orientation alignment, the fine-orientation alignment, and the position alignment, is working currently.

V. EXPERIMENTS AND RESULTS

A. Experiment System

An experiment system was established according to the scheme given in Section II-B, as shown in Fig. 12. In this experiment system, there were three microscopic cameras including two GC2450 cameras and one PointGrey camera. All three cameras equipped with Navitar zoom lens with magnification $0.47\text{--}4.5\times$, which captured images 15 frames/s with image size of 2448×2050 in pixel. The adjusting platform was composed Micos WT-100 for rotation around X_w - and Y_w -axis and Sigma SGSP-40YAW for rotation around Z_w -axis. The rotating resolution of the adjusting platform was 0.02° around Z_w -axis, 0.001° around X_w - and Y_w -axis, the translation reso-

lution was $1\text{ }\mu\text{m}$. The manipulator was Suguar KWG06030-G, whose translation resolution was $1\text{ }\mu\text{m}$ along X_w -, Y_w - and Z_w -axis, respectively. All three microscopes were placed on Sigma SGSP26-50 to move along their optical axes. The CPU of host computer was Intel Core2 DUO with frequency of 2.8 GHz.

B. System Calibration

The image Jacobian matrixes J_1 , J_2 , and J_3 were calibrated with the method presented in [13], which were given as following:

$$\begin{aligned} J_1 &= \begin{bmatrix} 0.0324 & -0.0041 & -1.1248 \\ 1.2243 & 0.0106 & -0.0214 \\ 0.1436 & -0.8846 & 0.1359 \end{bmatrix} \\ J_2 &= \begin{bmatrix} -0.3285 & -0.3828 & -0.0862 \\ -0.3839 & 0.3389 & -0.0701 \end{bmatrix} \text{ pixel}/\mu\text{m} \\ J_3 &= \begin{bmatrix} 0.1111 & -0.0840 & 0.0081 \\ 0.0071 & -0.0003 & -0.1561 \\ -0.0952 & -0.1248 & 0.0018 \\ -0.0001 & 0.0069 & -0.1782 \end{bmatrix} \text{ pixel}/\mu\text{m}. \end{aligned} \quad (16)$$

Additional experiments were conducted to validate the precision of the Jacobian matrices. First, the component A was actively rotated around X_w -axis for 1.00° , while its orientation around Y_w - and Z_w -axis was kept unchanged. The angle differences measured were -0.03° , 1.20° , and 0.16° by microscopic cameras 1, 2, and 3, respectively. Therefore, the orientation changes of the component A were calculated with the inverse of J_1 to be 0.98° around X_w -axis, -0.02° around Y_w -axis, and 0.06° around Z_w -axis.

Similarly, the component B was actively translated along X_{M2} -axis for $150\text{ }\mu\text{m}$, while its position along Y_{M2} -axis and Z_{M2} -axis was kept unchanged. The coordinate differences of the feature points extracted from cameras 2 and 3 were (16.7, 1.1) pixel and $(-14.3, 0.1)$ pixel, respectively. Therefore, the position changes of the component B were calculated with inverse of J_3 to be $150.3\text{ }\mu\text{m}$ for X_{M2} -axis, $-0.2\text{ }\mu\text{m}$ for Y_{M2} -axis and $-0.5\text{ }\mu\text{m}$ for Z_{M2} -axis.

The validation experiments demonstrate that the precision for orientation measurement was 0.1° and the precision for position measurement was $1\text{ }\mu\text{m}$.

As discussed in Section III-B, the direction vectors V_2 and V_3 of the optical axes of the microscopic cameras 2 and 3 with respect to the manipulator coordinates $\{M2\}$ were calibrated with (4). Their values were

$$\begin{aligned} V_2 &= [-5.0535 \quad -5.5885 \quad 1]^T \\ V_3 &= [4.9828 \quad -3.6540 \quad 1]^T. \end{aligned} \quad (17)$$

The view directions V'_2 and V'_3 of the microscopic cameras 2 and 3 with respect to microscopic camera 1 were computed

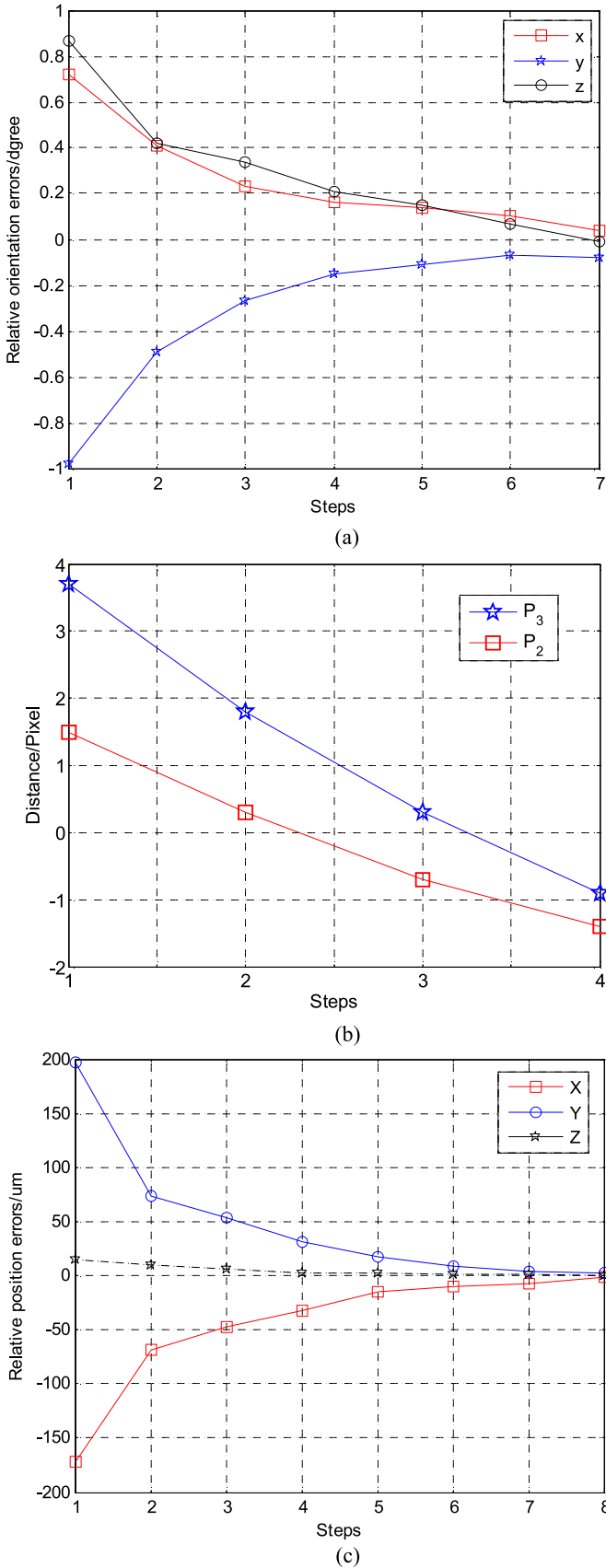


Fig. 13. Experimental results in alignment: (a) Orientation errors in coarse-orientation alignment, (b) distances from points involved in \mathcal{R} to groove lines \mathbf{L}_{ar} , and (c) position errors in position alignment.

TABLE I
DISPLACEMENT VECTORS

\mathbf{L}_{is1} and \mathbf{L}_{is2} relative to \mathbf{L}_{ia4} and \mathbf{L}_{ia5}	Displacement Vector
$[\Delta u_{2s1}, \Delta v_{2s1}]^T$	$[81.68, -9.21]^T$
$[\Delta u_{3s1}, \Delta v_{3s1}]^T$	$[-34.05, 3.84]^T$
$[\Delta u_{2s2}, \Delta v_{2s2}]^T$	$[47.05, 6.59]^T$
$[\Delta u_{3s2}, \Delta v_{3s2}]^T$	$[-43.31, -6.07]^T$

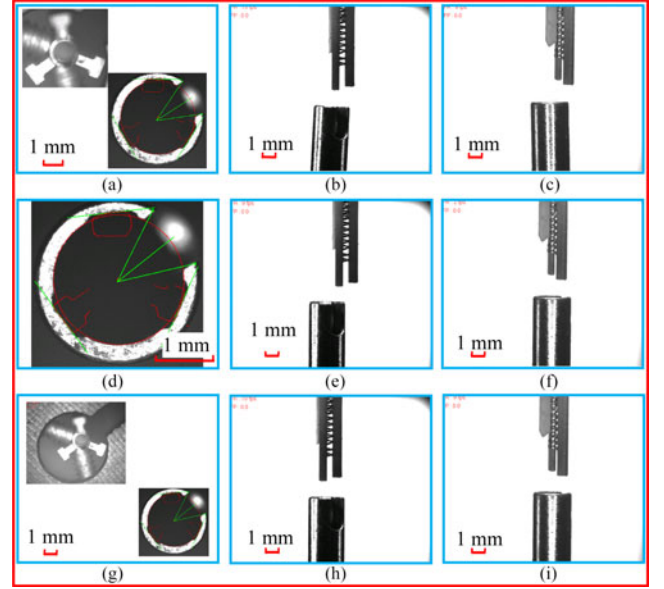


Fig. 14. Images in different stages, image captured by (a) microscopic camera 1, (b) microscopic camera 2 and (c) microscopic camera 3 before alignment, (d) microscopic camera 1, (e) microscopic camera 2, and (f) microscopic camera 3 after coarse-to-fine-orientation alignment, (g) microscopic camera 1, (h) microscopic camera 2, and (i) microscopic camera 3 after position alignment.

directly with the result given in

$$\mathbf{V}'_2 = \begin{bmatrix} -0.9999 \\ 0.0064 \end{bmatrix}$$

$$\mathbf{V}'_3 = \begin{bmatrix} -0.1005 \\ -0.9951 \end{bmatrix}. \quad (18)$$

C. Alignment Experiment

In the alignment experiments, the features were extracted as described in Section III-C. The threshold for the Canny operator was 100. The angle step length in PPHT for line detection was set to 0.05° , and the angle variation was limited in a small range of 10° . The PI control parameters were evaluated as follows $K_{p1} = 0.18$, $K_{i1} = 0.55$, $K_{p3} = 0.25$, $K_{i3} = 0.65$, and the ε for fine-orientation alignment was set 0.03° . The ε was set based on the image processing repeatability of orientation feature extraction. The expected aligning accuracy was 0.2° for orientation and $5 \mu\text{m}$ for position. The coarse-orientation alignment finished once the angle errors were less than 0.1° around \mathbf{X}_w , \mathbf{Y}_w , and \mathbf{Z}_w -axis. The fine-orientation alignment finished once $\Delta\theta_{c1}$

TABLE II
ADJUSTING STEPS AND CONVERGENCE ERRORS IN TEN EXPERIMENTS

no	Step		Errors		
	Orientation Alignment		Position Alignment	Orientation $\Delta\theta_x, \Delta\theta_y, \Delta\theta_z$ (Degree)	Position $\Delta x_{m2}, \Delta y_{m2}, \Delta z_{m2}$ (μm)
	Coarse	Fine			
1	7	4	8	0.04, -0.07, 0.01	1.2, -0.6, 1.7
2	8	2	8	-0.01, 0.04, 0.07	0.3, 1.6, -0.9
3	7	3	7	0.02, 0.06, -0.01	-0.6, 1.8, 1.1
4	9	1	9	0.07, 0.04, -0.03	-1.5, 0.7, 0.4
5	6	5	8	0.04, -0.07, 0.01	-1.1, 0.5, 0.7
6	8	3	11	-0.01, 0.08, 0.04	1.3, -0.9, 1.2
7	8	2	9	0.08, -0.07, 0.03	0.4, -0.5, 1.6
8	9	2	8	0.05, 0.06, -0.07	1.5, 1.1, -0.7
9	7	4	10	-0.06, -0.02, 0.08	0.3, -1.8, 0.7
10	9	3	7	0.02, -0.07, 0.04	0.9, -1.3, 1.5

computed by (12) was 0. The position alignment finished once the position errors of the component B relative to component A were less than $2 \mu\text{m}$ in Cartesian space along \mathbf{X}_w -, \mathbf{Y}_w -, and \mathbf{Z}_w -axis.

The alignment experiments including coarse-orientation alignment, fine-orientation alignment, and position alignment were well conducted more than 40 times with the proposed method in Section IV. Experimental results in one experiment were given in Fig. 13. Fig. 13(a) showed the relative orientation errors in coarse-orientation alignment. Fig. 13(b) showed the distances from points involved in \mathcal{R} to groove lines \mathbf{L}_{ar} in fine-orientation alignment. Fig. 13(c) showed the relative position errors in position alignment. With seven control steps, the orientation errors after coarse-orientation alignment around \mathbf{X}_w -, \mathbf{Y}_w - and \mathbf{Z}_w -axis were 0.04° , -0.07° , and 0.01° , respectively. After coarse-orientation alignment, $\Delta\theta_{c1}$ for fine-orientation alignment was computed. With four control steps, fine-orientation alignment is finished, and no limited lever corners were involved in the pixel set \mathcal{R} . Since (12) did not measure the relative orientation error around \mathbf{Z}_w -axis quantitatively, the distances from points \mathbf{P}_r and \mathbf{Q}_r , which were involved in \mathcal{R} , to groove lines \mathbf{P}_{ar} in fine-orientation alignment were given in Fig. 13(b). In the fine-orientation alignment, the points \mathbf{P}_2 and \mathbf{P}_3 were involved in \mathcal{R} . Fig. 13(b) showed the distance from the point \mathbf{P}_2 to the line \mathbf{L}_{a2} and the distance from the point \mathbf{P}_3 to the line \mathbf{L}_{a3} varied from positive to negative, and the point \mathbf{P}_2 and \mathbf{P}_3 were moved gradually from inside \mathcal{R} to outside \mathcal{R} . The negative distance in Fig. 13(b) meant the points were outside the \mathcal{R} .

After the coarse-to-fine-orientation alignment, the displacements of \mathbf{L}_{is1} and \mathbf{L}_{is2} relative to \mathbf{L}_{ia4} and \mathbf{L}_{ia5} were computed, $i = 2, 3$. The results were list in Table I.

With eight steps, the position errors along \mathbf{X}_w -, \mathbf{Y}_w - and \mathbf{Z}_w -axis were 1.2, -0.6, and $1.7 \mu\text{m}$, respectively. It can be seen from Fig. 13 that the whole control progress was performed smoothly and stably in alignment.

Fig. 14 showed the images captured by the three microscopic cameras before alignment, after coarse-to-fine-orientation

alignment, and position alignment in one alignment experiment. It can be found that the alignment achieved good results.

Ten times experiments under different initial conditions were well conducted. Table II showed the experimental results including the adjusting steps of alignment adjustment and the final adjusting convergence errors. The final orientation errors and the position errors were computed by the relative image feature errors and the image Jacobian matrix. The results in Table II demonstrated that the alignment of the long cylindrical component in 6-DOFs can be realized based on the relative pose estimation method in high repeatability with the orientation error less than 0.1° and the position error less than $2 \mu\text{m}$.

VI. CONCLUSION

The main contribution of this paper is the relative pose estimation method for long cylindrical components in 3-D Cartesian space with 6-DOF based on multimicroscopic vision. The axial dimension of the components is at least five times as large as their radial dimension so that they cannot be entirely perceived by the side-view cameras. The long cylindrical components are of prism shape with odd edges, whose central lines relative to the edge lines projected on the image plane vary with the projection directions. The main challenge in relative pose estimation is to determine the invisible feature lines for pose measurement. The relative pose estimation method proposed in this paper first estimates the relative orientation between components in a coarse-to-fine manner to provide higher orientation measurement accuracy. After the orientation alignment is finished, feature lines for position estimation are determined and the relative position between components is then estimated. The approach to determine the invisible feature lines for relative position error measurement between components is also presented. With the proposed relative pose estimation method, the alignment of long cylindrical components can be achieved with hardware system configuration requirements in which three microscopic cameras, a three translational DOFs manipulator, and a three rotational DOFs adjusting platform are needed.

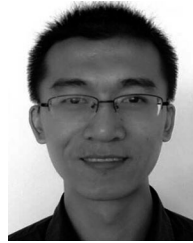
After alignment, a part (roughly 10% length) of the component B is inserted into the component A to verify whether the alignment errors were acceptable, by translating the component A along its rotation axis directly, and the successful rate in 40 insertion experiments is 100%.

In future, our work will be focused on the intelligent control methods in the insertion process of long cylindrical components.

REFERENCES

- [1] L. D. Wang, J. K. Mills, and W. L. Cleghorn, "Automatic microassembly using visual servo control," *IEEE Trans. Electron. Packag. Manuf.*, vol. 31, no. 4, pp. 316–325, Oct. 2008.
- [2] J. Fluitman, "Microsystems technology: Objectives," *Sens. Actuators A, Phys.*, vol. 56, pp. 151–166, 1996.
- [3] J. Zhang, D. Xu, Z. T. Zhang, and W. S. Zhang, "Position/force hybrid control system for high precision alignment of small gripper to ring object," *Int. J. Autom. Comput.*, vol. 10, no. 4, pp. 360–367, Aug. 2013.
- [4] H. V. Brussel, J. Peirs, D. Reynaerts, A. Delchambre, G. Reinhart, N. Roth, M. Weck, and E. Zussman, "Assembly of microsystems," *Ann. CIRP*, vol. 49, no. 2, pp. 451–472, 2000.

- [5] J. A. Franklin and H. Benbrahim, "Acquiring robot skills via reinforcement learning," *IEEE Control Syst.*, vol. 14, no. 1, pp. 13–24, Feb. 1994.
- [6] W. Gerum, M. Bruck, and G. Fischer, "Space qualified low/high-power radar TWTs," *IEEE Trans. Electron. Devices*, vol. 5, no. 5, pp. 669–672, May 2005.
- [7] H. Gong, Y. Gong, T. Tang, J. Xu, and W. Wang, "Experimental investigation of a high-power Ka-band folded waveguide traveling-wave tube," *IEEE Trans. Electron. Devices*, vol. 58, no. 7, pp. 2159–2163, Jul. 2011.
- [8] Y. Han, Y. Liu, Y. Ding, and C. Lu, "Thermal analysis of helix TWT slow-wave structure," *IEEE Trans. Electron. Devices*, vol. 55, no. 5, pp. 1269–1272, May 2008.
- [9] Y. Han, Y. Liu, and Y. Ding, "An evaluation of heat dissipation capability of the slow-wave structures," *IEEE Trans. Electron. Devices*, vol. 54, no. 6, pp. 1562–1565, Jun. 2007.
- [10] Y. Han, Y. Liu, Y. Ding, and P. Liu, "Improvement of heat dissipation capability of slow-wave structure using two assembling methods," *IEEE Electron. Device Lett.*, vol. 29, no. 8, pp. 955–956, Aug. 2008.
- [11] L. Wang, L. Ren, J. K. Mills, and W. L. Cleghorn, "Automated 3-D micrograsping tasks performed by vision-based control," *IEEE Trans. Autom. Sci. Eng.*, vol. 7, no. 3, pp. 417–426, Jul. 2010.
- [12] F. Shen, W. Wu, D. Yu, D. Xu, and Z. Cao, "High precision automated 3-D assembly with attitude adjustment performed by LMTI and vision based control," *IEEE Trans. Mechatronics*, vol. 20, no. 4, pp. 1777–1789, Aug. 2015.
- [13] S. Liu, D. Xu, D. Zhang, and Z. Zhang, "High precision automatic assembly based on microscopic vision and force information," *IEEE Trans. Autom. Sci. Eng.*, to be published, doi: 10.1109/TASE.2014.2332543.
- [14] A. Ferreira, C. Cassier, and S. Hirai, "Automatic microassembly system assisted by vision servoing and virtual reality," *IEEE/ASME Trans. Mechatronics*, vol. 9, no. 2, pp. 321–333, Jun. 2004.
- [15] Z. Zhang, J. Zhang, and D. Xu, "Design of microassembly system and research on coarse-to-fine alignment strategy in combination with active zooming," in *Proc. IEEE Workshop Robot. Vis.*, Jan. 2013, pp. 76–81.
- [16] M. Subbarao and J. K. Tyan, "Selecting the optimal focus measure for autofocusing and depth-from-focus," *IEEE Trans. Pattern Anal. Mach. Intell.*, vol. 20, no. 8, pp. 864–870, Aug. 1998.
- [17] S. Wang and S. Yang, "Research of depth information acquisition with two stage structured light method," in *Proc. IEEE Int. Conf. Prog. Informat. Comput.*, 2000, vol. 2, pp. 800–803.
- [18] W. Yuan, G. Jiang, Y. Wang, M. Yu, F. Shao, and Z. Peng, "Grid-based corner detection of the microscopic camera calibration," *Adv. Mater. Res. Adv. Meas. Test*, vols. 301–303, pp. 1145–1150, 2011.
- [19] D. Xu, F. Li, Z. Zhang, Y. Shi, H. Li, and D. Zhang, "Characteristic of monocular microscope vision and its application on assembly of micro-pipe and micro-sphere," in *Proc. 32nd Chin. Control Conf.*, Jul. 2013, pp. 5758–5763.
- [20] L. Ren, L. Wang, J. K. Mills, and D. Sun, "3-D automatic microassembly by vision-based control," in *Proc. IEEE Int. Conf. Intell. Robots Syst.*, Oct./Nov. 2007, pp. 297–302.
- [21] X. Huang, S. Mao, and M. Wang, "A novel visual servoing microassembly system," in *Proc. IEEE 2nd Int. Conf. Cloud Comput. Intell. Syst.*, 2012, vol. 2, pp. 966–970.
- [22] E. Rublee, V. Rabaud, K. Konolige, and G. Bradski, "ORB: An efficient alternative to SIFT or SURF," in *Proc. IEEE Int. Conf. Comput. Vis.*, New York, NY, USA, 2011, pp. 2564–2571.
- [23] J. T. Feddema and R. W. Simon, "CAD-driven microassembly and visual servoing," in *Proc. IEEE Int. Conf. Robot. Autom.*, 1998, vol. 2, pp. 1212–1219.
- [24] X. Tao, F. Janabi-Sharifi, and H. Cho, "An active zooming strategy for variable field of view and depth of field in vision-based microassembly," *IEEE Trans. Autom. Sci. Eng.*, vol. 6, no. 3, pp. 504–513, Jul. 2009.
- [25] L. Ren, L. Wang, J. K. Mills, and D. Sun, "Vision-based 2-D automatic micrograsping using coarse-to-fine grasping strategy," *IEEE Trans. Ind. Electron.*, vol. 55, no. 9, pp. 3324–3331, Sep. 2008.
- [26] H. K. Chu, J. K. Mills, and W. L. Cleghorn, "Fabrication of a microcoil through parallel microassembly," in *Proc. IEEE Int. Conf. Robot. Autom.*, St. Paul, MN, USA, May 14–18, 2012, pp. 5050–5055.
- [27] C. Galambos, J. Kittler, and J. Matas, "Gradient-based progressive probabilistic Hough transform," *IEEE Vis. Image Signal Process.*, vol. 148, no. 3, pp. 158–165, 2002.
- [28] J. Canny, "A computational approach to edge detection," *IEEE Trans. Pattern Anal. Mach. Intell.*, vol. PAMI-8, no. 6, pp. 679–714, Nov. 1986.
- [29] Q. Zhu, L. Jing, and R. Bi, "Exploration and improvement of Ostu threshold segmentation algorithm," in *Proc. 8th World Congr. Intell. Control Autom.*, Jul. 2010, pp. 6183–6188.
- [30] D. Xu, M. Tan, Y. Liu, and J. Wang, "Control strategy for a low cost manipulator to transport and align IC mask-plates," *IEEE Trans. Control Syst. Technol.*, vol. 17, no. 5, pp. 1018–1027, Sep. 2009.
- [31] D. Xu, F. Li, Z. Zhang, Y. Shi, H. Li, and D. Zhang, "Characteristic of monocular microscopic vision and its application on assembly of micro-pipe and micro-sphere," in *Proc. 32nd Chin. Control Conf.*, Xi'an, China, Jul. 26–28, 2013, pp. 5758–5763.



Song Liu received the B.Sc. degree in sensing technology and instrumentation from Shandong University, Jinan, China, in 2012. He is currently working toward the Ph.D. degree in control science and engineering at the Institute of Automation, Chinese Academy of Sciences, Beijing, China.

His current research interests include visual measurement, visual control, visual positioning, and microassembly.



De Xu (M'05–SM'09) received the B.Sc. and M.Sc. degrees in control science and engineering from the Shandong University of Technology, Jinan, China, in 1985 and 1990, respectively, and the Ph.D. degree in control science and engineering from Zhejiang University, Hangzhou, China, in 2001.

Since 2001, he has been with the Institute of Automation, Chinese Academy of Sciences, Beijing, China, where he is currently a Professor at the Research Center of Precision Sensing and Control. His current research interests include robotics and automation, such as visual measurement, visual control, intelligent control, welding seam tracking, visual positioning, microscopic vision, and microassembly.



Fangfang Liu received the B.S. and Ph.D. degrees in mechanical electronics from Zhejiang University, Hangzhou, China, in 2006 and 2012, respectively.

She is currently an Associate Professor at the Research Center of Precision Sensing and Control, Institute of Automation, Chinese Academy of Sciences, Beijing, China. Her research interests include precision mechanical design and mechatronic control.



Dapeng Zhang received the B.Sc. and M.Sc. degrees from the Hebei University of Technology, Tianjin, China, in 2003 and 2006, respectively, and the Ph.D. degree from the Beijing University of Aeronautics and Astronautics, Beijing, China, in 2011.

He is currently an Associate Professor at the Research Center of Precision Sensing and Control, Institute of Automation, Chinese Academy of Sciences, Beijing. His research interests include robotics and automation, in particular medical robot and virtual robotic surgery.



Zhengtao Zhang (M'12) received the B.Sc. degree in control science and engineering from the China University of Petroleum, Dongying, China, in 2004, the M.Sc. degree in control science and engineering from the Beijing Institute of Technology, Beijing, China, in 2007, and the Ph.D. degree in control science and engineering from the Institute of Automation, Chinese Academy of Sciences (IACAS), Beijing, in 2010.

He is currently a Professor at the Research Center of Precision Sensing and Control, IACAS. His research interests include visual measurement, microassembly, and automation.